


**Gapless dispersion of acoustic line modes with glide symmetry**Gareth P. Ward,<sup>1</sup> John D. Smith,<sup>2</sup> Alastair P. Hibbins,<sup>1</sup> J. Roy Sambles<sup>1</sup> ,<sup>1</sup> and Timothy A. Starkey<sup>1</sup><sup>1</sup>*Centre for Metamaterial Research and Innovation, University of Exeter, Exeter EX4 4QL, United Kingdom*<sup>2</sup>*DSTL, Porton Down, Salisbury, Wiltshire SP4 0JQ, United Kingdom*

(Received 19 October 2020; revised 16 May 2022; accepted 19 May 2022; published 1 June 2022)

The effect of glide symmetry on the dispersion of acoustic surface waves supported by lines of open-ended holes in acrylic plates is investigated. Two samples are experimentally characterized, each formed of a pair of such parallel lines, one having glide-symmetry. This glide symmetry removes the condition necessary for the supported even and odd character acoustic surface waves to form standing waves at the first Brillouin zone boundary; there is instead one mixed even-odd hybrid mode. This evolves continuously with increasing frequency to a far greater in-plane wave vector than possible without the glide condition. This paper demonstrates that glide symmetry opens a degree of freedom for the design of acoustic metamaterial devices for the control of acoustic energy on a surface.

DOI: [10.1103/PhysRevB.105.245401](https://doi.org/10.1103/PhysRevB.105.245401)**I. INTRODUCTION**

Over the past decade, acoustics-based research has had somewhat of a renaissance, with much study being directed toward the exploration of acoustic metamaterials for the control of airborne sound. Inspired by similar research in the electromagnetic domain [1], these materials have acoustic responses dictated by macroscopic structuring rather than by microscopic molecular properties, allowing them to be used to manipulate sound in unusual ways [2,3]. A subset of these materials rely on the presence of the acoustic surface wave (ASW) (sometimes termed leaky guided modes [4] or spoof surface acoustic waves [5]), a trapped surface wave existing purely within the air, resonant in the cavities, and evanescently decaying away from the boundary of the metamaterial [6–8]. These can be considered analogous to spoof Surface Plasmon Polaritons (SSPPs), which mimic the characteristics of surface plasmon polaritons on a structured surface [9–11]. Typically, this ASW is supported on a periodically arranged set of identical resonant cavities, formed within a solid that can be considered perfectly rigid to an acoustic wave within the air. The Fabry-Pérot-like cavity modes that arise due to the impedance mismatch at the ends of each rigid-walled cavity couple together over the surface of the periodic structure via near-field diffraction and create an effective impedance condition that supports a localized surface mode [4,12–20].

The behavior of SSPPs on similarly structured electromagnetic metamaterials is well understood [21]. A periodic subwavelength array of cavities in a perfect electrical conducting substrate supports localized SSPPs that have fields that decay exponentially away from the interface into both cavities below, and air above, with the electromagnetic fields localized at the cavities [22]. This is parallel to the acoustics case, where the pressure fields are also localized at the cavities [14]. For both Fabry-Pérot-like ASWs and SSPPs, as the in-plane wave vector approaches the edge of the first Brillouin zone (BZ)

(at a wave vector dictated by the periodicity of the grating), the group velocity falls to zero due to Bragg diffraction. The supporting structures produce mode dispersions described by well-established solid-state physics for wave propagation in periodic systems [23].

In air, such ASWs supported by perforated rigid structures underpin a range of acoustic phenomena, including enhanced acoustic transmission ([13,24,25], subwavelength imaging [26,27], and collimation and focusing [5,28,29]. In the hydroacoustic domain, studies have examined the influence of ASWs on the radiation of Lamb modes [30,31], and there have been studies of these nonradiative surface waves supported by one-dimensional (1D) arrays of water-filled grooves [14] and two-dimensional (2D) arrays of material-filled holes [32]. Furthermore, Hou *et al.* showed that it is possible to excite underwater ASWs supported by a simple square array of holes in a metal plate [13], and even when the supporting solid is elastic [19]. ASWs have also been suggested as a means to sense the temperature [33] and the chemical composition of the fluid in which the wave propagates [34], and have been proposed as a route for controlling fluid flow [35].

In the present paper, the ease of manipulation of the acoustic line mode (ALM) that exists on a simple line of holes [36,37] is exploited to form a compound grating that supports a high- and low-energy standing-wave pair. A type of higher symmetry known as glide symmetry [38,39] is then introduced, its effect such that the standing wave that each individual ASW would normally form at the first Brillouin zone boundary (BZB) is forbidden. This allows the ASWs to have a much larger frequency band of gapless dispersion, reaching a similarly increased in-plane wave vector. Similar work has been reported by some of the present authors, where they investigated the glide-symmetry effect in the case of a single, snaking acoustic waveguide [17], which has other considerations such as the existence of a waveguide cutoff frequency. Further research has been proposed using closed

meander-like acoustic waveguides with glide symmetry as a platform for acoustic sensing utilizing Mach-Zender interferometry principles [40]. Unlike these studies, which rely on a waveguide structure, here we are concerned with the purely surface modelike behavior of ASWs. Via characterization of the acoustic near-field for each sample, high-resolution 2D acoustic pressure maps are created, from which spatial fast-Fourier-transform algorithms extract the dispersion relations of the trapped surface modes. These ASW-supporting structures may readily be fabricated so the ASW exists over the audible range, hence they may be useful for the design of devices for confining and controlling sound such as acoustic lenses [5], matched layers, or leaky wave antennas [41].

## II. GLIDE SYMMETRY

If the periodicity  $\lambda_g$  of a system is along  $x$  and this system also has some structure-factor component in  $y$ , glide symmetry is defined as a system that is invariant under an inversion in the  $y$  dimension along its  $y$  midplane, except for a shift of exactly half its periodicity  $\lambda_g/2$  along  $x$ . Many commonly found shapes have this property, such as a zigzag or a simple sine wave. The glide operator  $G$  can be stated mathematically as

$$G = \begin{cases} x \rightarrow x + \frac{\lambda_g}{2} \\ y \rightarrow -y \\ z \rightarrow z. \end{cases} \quad (1)$$

A generalized Floquet theory of electromagnetic systems with glide symmetry has been developed in an extensive study by Hessel *et al.* [38], which, along with McWeeny's treatise regarding symmetry and crystal band structure [42], has since formed the basis for much research in this area. Hessel *et al.*'s [38] work predicts that glide symmetry can have a significant effect on the dispersion of surface modes. Summarized briefly, if a patterned electromagnetic waveguide containing periodic structure is rearranged to become glide symmetric, two modes that were originally separate with different energies, one having even character (symmetric about the cavity mirror plane), and one odd (antisymmetric about the mirror plane), will form a single mode of mixed character. As separate even and odd modes, they interact with modes diffracted from  $k_x = k_g$  (where the grating wave vector  $k_g = 2\pi/\lambda_g$ ) to form standing waves at the first BZB,  $k_x = k_g/2$ , with a frequency band gap between them. By displacing the position of the field antinodes by exactly half a unit cell, the glide symmetry forces the even and odd modes to mix with no standing wave or band gap forming at the first BZB. This mode instead forms a standing wave at some arbitrary point in  $k$  space shifted from the BZB, but before crossing the second BZB at  $k_x = k_g$ . This surface mode of mixed character is thus capable of reaching in-plane wave vectors beyond the first BZ with no discontinuities in its dispersion.

In the optical-electromagnetic case, the interaction of surface plasmons (a type of electromagnetic trapped surface wave) with diffraction gratings that have glide symmetry has been studied before. Constant *et al.* [43] characterized the surface-plasmon dispersion on a zigzag grating and confirmed that the dispersion of the surface plasmon becomes gapless at the first BZ boundary in such a system. Similarly,

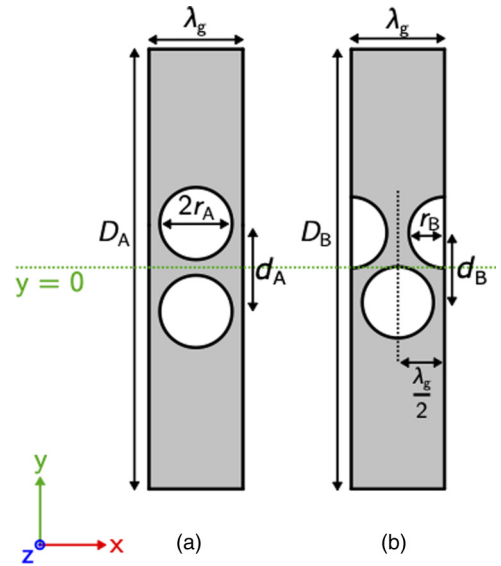


FIG. 1. 2D schematic of both unit cells that make up each of the full length samples A and B, depicted in Fig. 2, where grey represents the acrylic and white space air. Both samples have periodicity  $\lambda_g = 8 \pm 0.01$  mm along  $x$ . A is the sample consisting of two adjacent open-ended holes of radius  $r_A = 3.20 \pm 0.05$  mm, with hole centres spaced  $d_A = 7 \pm 0.01$  mm apart in  $y$ , the acrylic plate being  $D_A = 36.30 \pm 0.05$  mm wide. Sample B has acrylic plate width  $D_B = 35.55 \pm 0.05$  mm, and radius of holes  $r_B = r_A$ , but, compared to sample A, the top line of holes are all shifted by  $\lambda_g/2$  in  $x$ , and hole centers are separated by  $d_B = 6 \pm 0.01$  mm in  $y$  (thus with total displacement between centers  $7.21 \pm 0.01$  mm).

Quesada *et al.* [39] studied glide symmetry in the microwave regime and found that the gapless dispersion of surface plasmons within a waveguide possessing glide-symmetry enabled regions of subwavelength negative dispersion. Here, the effect that glide symmetry has on ASWs is investigated, with conclusions drawn in part by using analogies to the aforementioned electromagnetic research.

## III. SAMPLE DESIGN AND EXPERIMENTAL METHOD

Figure 1 is a schematic of the unit cells that make up each periodic sample, while Fig. 2 depicts the samples in their entirety. In each case, important dimensions are labeled. Both samples were laser cut into acrylic plates and consist of 105 periodic unit cells of grating pitch  $\lambda_g$ , thereby providing an adequate approximation to an infinitely periodic system. Sample A consists of two adjacent lines of circular holes, which are symmetric in the unit cell's  $y$  mirror plane, providing a contrast to sample B, where one of the lines of holes is shifted along  $x$  by  $\lambda_g/2$  and thus the unit cell has glide symmetry. Also, the  $y$  separation of holes in sample B has been made as small as the manufacturing process allows, both to increase the diffractive coupling strength between fields of the two lines of holes, and make hole-center-to-hole-center displacements as close as possible to those of sample A. For both samples, the acrylic thickness and thus hole depth is  $H = 9.7 \pm 0.2$  mm, placing the fundamental resonant wavelength at  $\lambda_{FP} \approx 2H = 19.6$  mm. This is more than twice the grating pitch  $\lambda_g = 8$  mm and thus they are short-pitch gratings. Also,

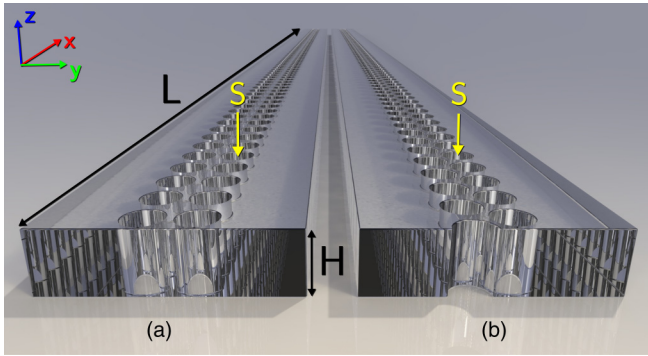


FIG. 2. Schematic of the acrylic samples, which have 210 open-ended cavities laser cut into them. The length of both samples is  $L = 840$  mm, with thickness  $H = 9.7 \pm 0.2$  mm. The position of the pointlike source of excitation is marked on each sample by the yellow arrow labeled S.

this plate thickness places the cavities' resonant frequencies in the 10 – 15 kHz range, making them possible to both excite and measure with widely available audio equipment.

To characterize the dispersion of each sample, an acoustic near-field measurement technique was utilized (details described in Appendix A). The samples' surface planes were aligned with a motorized XY stage that has a probe microphone attached, its 1 mm diameter aperture spaced  $<1$  mm from each sample surface. The motors are programed to move the microphone in a precise grid of  $x$  and  $y$  coordinates, with an error in position of  $<10 \mu\text{m}$ . At each point, the microphone records the average value of a series of Gaussian pulses emitted by a pointlike source, which is placed inside one of the holes at a position near the sample end in  $L$ , as marked by S in Fig. 2. The source was not placed directly within a hole on the sample edge, as reflections from the impedance mismatch presented by this edge could interfere with the recorded signal. Placing the source inside a hole further along in  $x$  significantly reduced the contribution of these weak reflections by both delaying them in time and reducing their amplitude. Also, the sample was longer in  $x$  than the XY stage's available scanning length, ensuring maximum possible  $x$  scan length and thus spatial frequency resolution  $k_x$ . The resulting time-domain signals for each point are converted to the frequency domain via a 1D Fourier transform, then combined to make detailed 2D real-space pressure field maps from which dispersions can be extracted via 2D spatial Fourier transform algorithms. The resolution in  $(x, y)$  recorded for each sample in each case is  $\Delta x = \Delta y = 0.5$  mm  $\ll \lambda_g$ , preventing the occurrence of aliasing in the regions of interest of the reciprocal space maps produced by the spatial Fourier transform analysis. For both samples, the standard techniques of zero-padding and Hanning-window functions are applied to the 2D real-space data matrices to reduce Fourier transform artifacts while artificially enhancing  $k$ -space resolution.

#### IV. RESULTS AND DISCUSSION

To understand how glide symmetry changes the dispersion of an ASW, first a system which does not possess it but that is otherwise identical to one which does is characterized. Sample

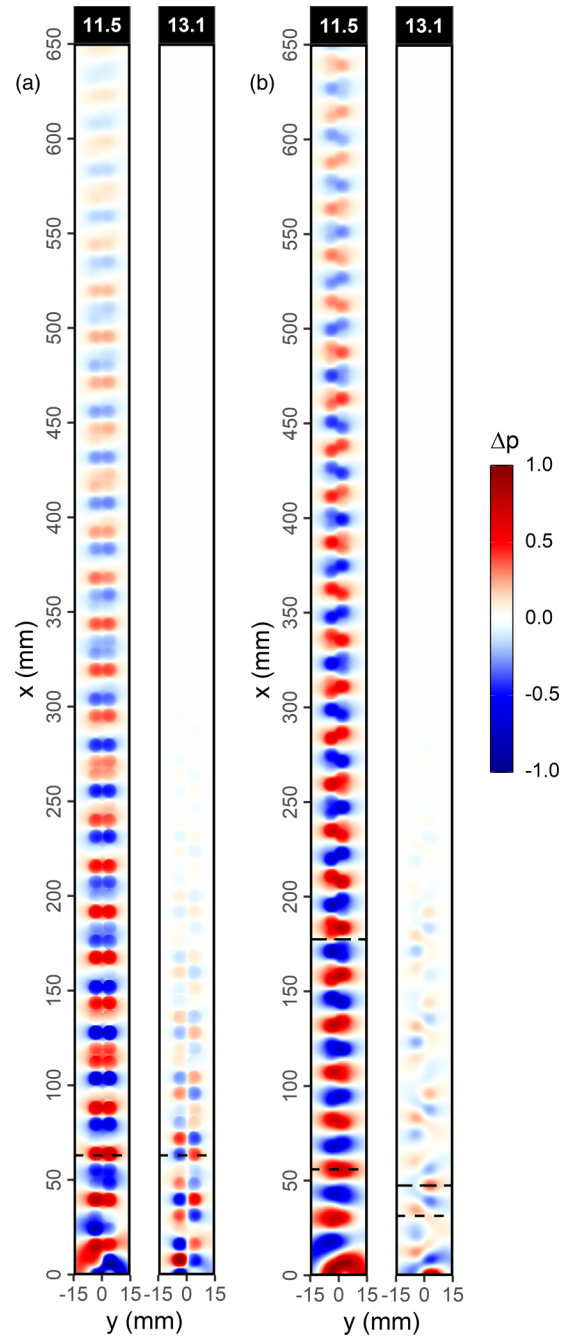


FIG. 3. 2D real-space plots of the experimentally measured instantaneous pressure field amplitude  $\Delta p$  at two separate frequencies (11.5 and 13.1 kHz, as labeled) for (a) sample A and (b) sample B. Pressure fields have been normalized to their maximum amplitude for each individual frequency. The pointlike source was located in the open-ended hole at  $x = 0$  mm,  $y = 4$  mm for sample A, and at  $x = 0$  mm,  $y = -3$  mm for sample B. The spatial resolution is  $\Delta x = \Delta y = 0.5$  mm for both sample measurements. The dashed lines indicate positions for which cross sections of the fields are discussed in the text.

A provides this comparison. Figure 3(a) shows the experimentally recorded instantaneous pressure field amplitude  $\Delta p$  of sample A at two frequencies 11.5 kHz and 13.1 kHz, which correspond to ratios of grating pitch to free-space wavelength

of  $\frac{\lambda_g}{\lambda_0} = 0.26$  and  $0.30$ , respectively. The shape of the individually excited cavities is very clear in both images despite them having a radius much smaller than the excitation wavelength; the acoustic near-field is being measured.

In recent work by the current authors [36], it was shown that a single line of holes was all that was required to excite an ASW in the form of an acoustic line mode. Since a full 2D hole array also supports an ASW [4,16,26], it follows that two adjacent lines of holes will support one, as this configuration falls between the extremes of the line array and the square array. The lower frequency shown in Fig. 3(a) confirms this, being at a frequency where the fundamental ASW is strongly excited. This frequency is not quite at the frequency where a standing wave could form, but the phase shift between cavities in the  $x$  direction is clear. The other important detail is that the pressure fields in each pair of holes are in phase with each other, as marked by the black dashed line at  $x = 57$  mm. Hence, across the  $y$ -dimension mirror plane, at this frequency the ASW is symmetric, i.e., it has even character.

A key difference between this sample and both the square-array and line-array samples previously studied [26,36] is that the unit cell here contains two resonant cavities, not just one. As seen in previously studied compound slit-array structures [44], this means that there should be an extra degree of freedom available to the near field, allowing a mode that resembles a phase resonance (i.e., the fields in the cavities within a single unit-cell couple together, but with a significant phase-shift between them) to become excitable. Indeed, this is the mode excited at the higher frequency in Fig. 3(a). Inspection of the fields shows that not only is there a clear phase shift between cavities along the  $x$  direction but also that there is a  $\pi$  phase shift between pairs of cavities in the  $y$  direction (also marked by a black dashed line at  $x = 63$  mm); this mode is antisymmetric in  $y$ , i.e., it has odd character. Another difference between the fields of the two frequencies is the decay length in the direction of ASW propagation  $x$ , where the low-frequency even mode has a much longer amplitude decay length than the high-frequency odd one. This is partly because, as will be seen in the dispersions to be discussed forthwith, the odd mode must have a finite  $k_y$  component as well as  $k_x$  and  $k_z$ . The pressure field plots are not definitive, however; the choice of frequency may place one of these modes closer to its standing-wave condition, where the group velocity necessarily decreases and so too the propagation distance. For both frequencies, the presence of the sample edge across dimension  $D_A$  is visible, as the change in surface impedance causes a reflection but, as with the line samples previously studied [36], it is not expected that this will have a significant effect on the dispersion of the ALMs.

With the nonglide symmetric sample examined, the effect that glide symmetry has on the mode dispersion can be isolated. Figure 3(b) shows the experimentally measured pressure fields for sample B at frequencies 11.5 and 13.1 kHz, the same as for sample A. Many of the same features are visible, such as the strong localization of the field above individual holes, and the reduction in intensity as  $x$  increases. However, there is a fundamental difference between the high and low frequencies compared with sample A. In the previous case, there was a clear change in behavior between the high- and low-frequency modes, where the low-frequency one had even

character (phase of the holes' pressure fields  $\Delta p$  symmetric in the  $y$  mirror plane) and the high-frequency one odd character (a  $\pi$  phase shift across the fields in the  $y$  mirror plane). For the glide-symmetric sample shown here, one cannot make this distinction. For both frequencies, at some cross section of  $y$ , the excited ALM has both even and odd character. The low-frequency mode generally has more even character, such as the point marked with a short-dashed line at  $x = 56$  mm, whereas at a different cross section such as that marked by the long-dashed line at  $x = 178$  mm, it appears to have odd character. Similarly, the high-frequency mode has mostly odd character, such as at the cross section marked by the long dashed line at  $x = 48$  mm, with some areas of even character, again marked by the short-dashed line at  $x = 32$ . These frequencies represent the two extremes, the change in behavior evolves as a continuum between them. Not included here, a field plot at a frequency chosen such that this hybrid mode has a wave vector approaching the first BZ would show that the two types of character become very hard to distinguish. Other important changes in behavior become clear in the corresponding  $k$ -space and dispersion diagrams.

Inspection of the reciprocal-space maps of the surface modes reveals much about their nature and differences between samples A and B. In Fig. 4 are the reciprocal-space (or  $k$ -space) plots that resulted from spatial Fourier transforms of the experimentally recorded pressure fields in Fig. 3, truncated to show only the first three BZs (which are in this case 1D), and with important features marked such as the sound circle  $k_0 = \sqrt{k_x^2 + k_y^2} = \frac{2\pi f}{c}$ , the maximum in-plane wave vector that a radiative sound-wave can possess.

First, for sample A, the low-frequency  $k$ -space map is markedly similarly to the equivalent plot seen for the simple line-array sample in the prior study [36] in that there is a clear, bright,  $k_y$ -independent feature that exists in the nonradiative regime of the first BZ ( $k_x > k_0$  and  $k_x < k_g/2$ ). This even-character ALM's strongest amplitude is at  $\frac{k_y}{k_g} = 0$ , and there is a sudden drop in amplitude visible at  $\frac{k_y}{k_g} = 0.6$  that corresponds to the total width of 13.4 mm formed by the combination of each holes' diameter and their separation in  $y$ . Features that result from the diffraction of the ALM are present just outside the diffracted sound circles at  $\frac{k_x}{k_g} = \pm 1$ , having identical character to the original. There is also a weak feature within the first BZ in the negative half of  $k$  space, which is the result of a reflection from the end of the sample exciting the ALM that propagates in the opposite direction.

The higher frequency  $k$ -space plot in Fig. 4(a) (right) has some features of interest. First, the ALM that was present in the low-frequency  $k$ -space plot is no longer visible (this is confirmed via inspection of the dispersions in Fig. 5, to be discussed). Second, the strong feature that is visible has a sudden drop in amplitude near  $\frac{k_y}{k_g} = 0$ , in contrast to the low-frequency mode which has a maximum at that point. This feature thus corresponds to the ALM with odd (or antisymmetric) character not excitable without some component of  $k_y$ , since it requires a  $\pi$  phase change orthogonal to the  $x$  axis. This mode still does not appear to disperse in the  $k_y$  direction as there is no  $y$  periodicity, but the pattern of its amplitude is significantly different from the low frequency even mode.

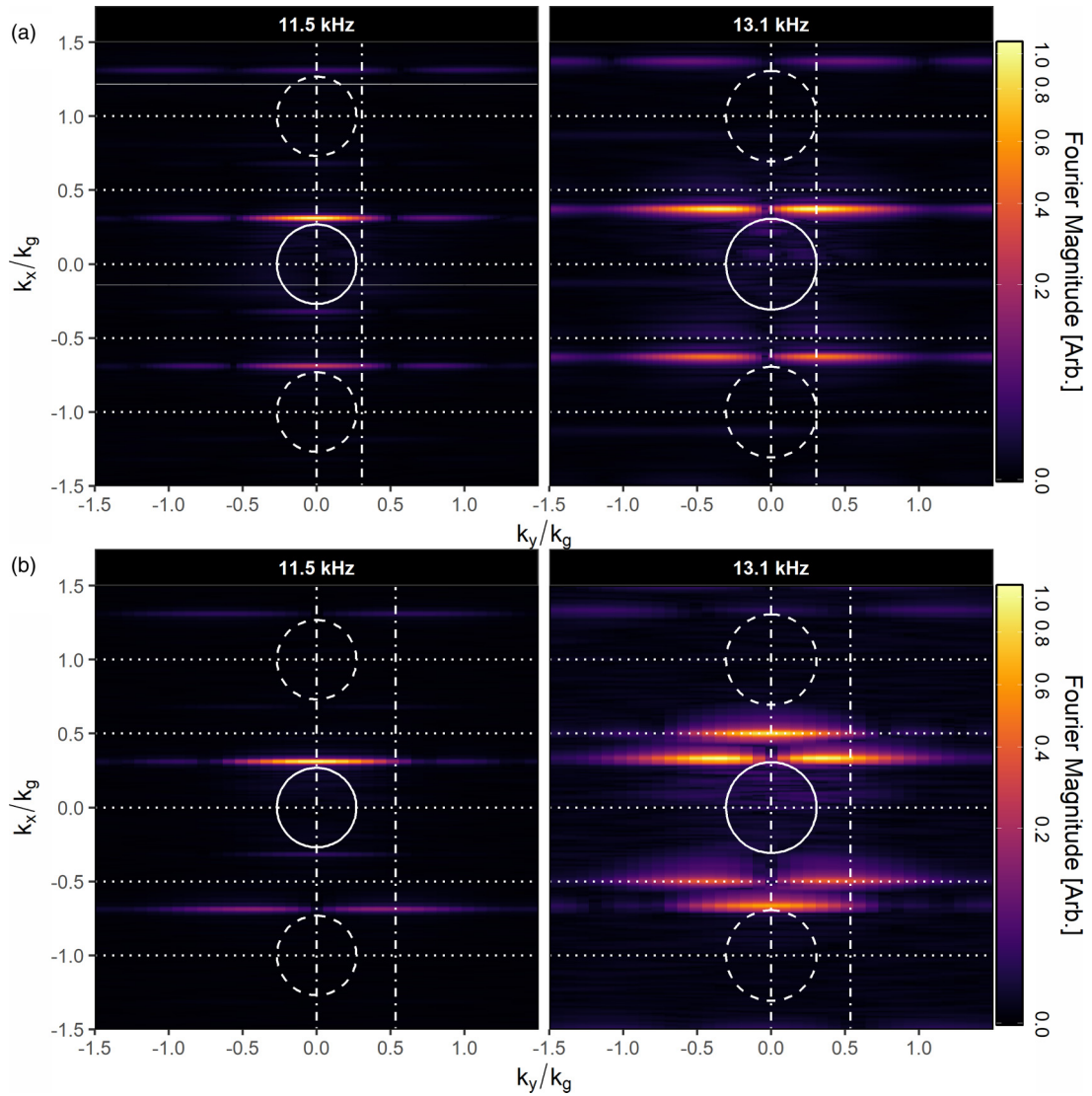


FIG. 4. 2D  $k$ -space plots corresponding to the pressure field plots in Fig. 3 for (a) sample A and (b) sample B (oriented in the same way). Wave vectors  $k_x$  and  $k_y$  are scaled to grating wave vector  $k_g$ , with the color scale representing the magnitude of Fourier components. The solid white circle represents the sound circle  $k_0 = \sqrt{k_x^2 + k_y^2} = \frac{2\pi f}{c}$ , the dashed circles  $k_0 \pm nk_g$ . Dotted horizontal lines are Brillouin zone boundaries  $\pm \frac{nk_g}{2}$ . Dot-dashed vertical lines are the cross sections of  $k_y$  used to create dispersion plots in Fig. 5.

The other facet of the oddlike mode's behavior to remark upon is its existence in the first BZ and not the second, unlike the antisymmetric phase-resonant ASWs on the compound grating structures studied in previous work [44–46]. This is because, although there is an extra degree of freedom available to the acoustic near-field, it is along  $y$  and not  $x$ , thus it does not enable the mode to reach a higher in-plane wave vector  $k_x$  than a simple line-array sample. A higher frequency mode can exist due to the extra  $k_y$  component of the grating's Fourier coefficients, but not at a higher wave vector  $k_x$ .

Figure 4(b) shows the  $k$ -space plots of the fields in Fig. 3(b), with all of the marked features having the same meaning as they did in Fig. 4(a). Once again, there are some features similar to those in the nonglide symmetric sample A. First, for the low frequency, there is a bright, flat feature within the first BZ but outside of the sound circle that corresponds to the trapped ALM. Its peak amplitude is at  $\frac{k_y}{k_g} = 0$ , and a

sudden drop in intensity is visible at  $\frac{k_y}{k_g} = 0.6$  that again stems from the combined diameter and separation of the open holes in the  $y$  dimension. The two modes visible that correspond to the diffraction from  $\pm k_g$  of the original, have a substantial change in their behavior. These modes have a strong  $k_y$  dependence, implying that some finite component of  $k_y$  is required to excite the diffracted order but not the original. This is the character that only the odd mode had in the dispersion of sample A, showing that the two modes have now mixed to create a new hybridized mode. This aspect of the mode dispersion implies that the glide symmetry has removed diffraction in the  $x$  plane alone, and as explained by Hessel *et al.* [38], this is due to a destructive phase cancellation resulting from the shift of the holes along  $x$ . This is the same reason that this mode does not now form a standing wave at the first BZB [(visible in Figs. 3(b) and 5(b), to be discussed)]; the pressure antinodes that would form a standing wave along one of the pair of holes

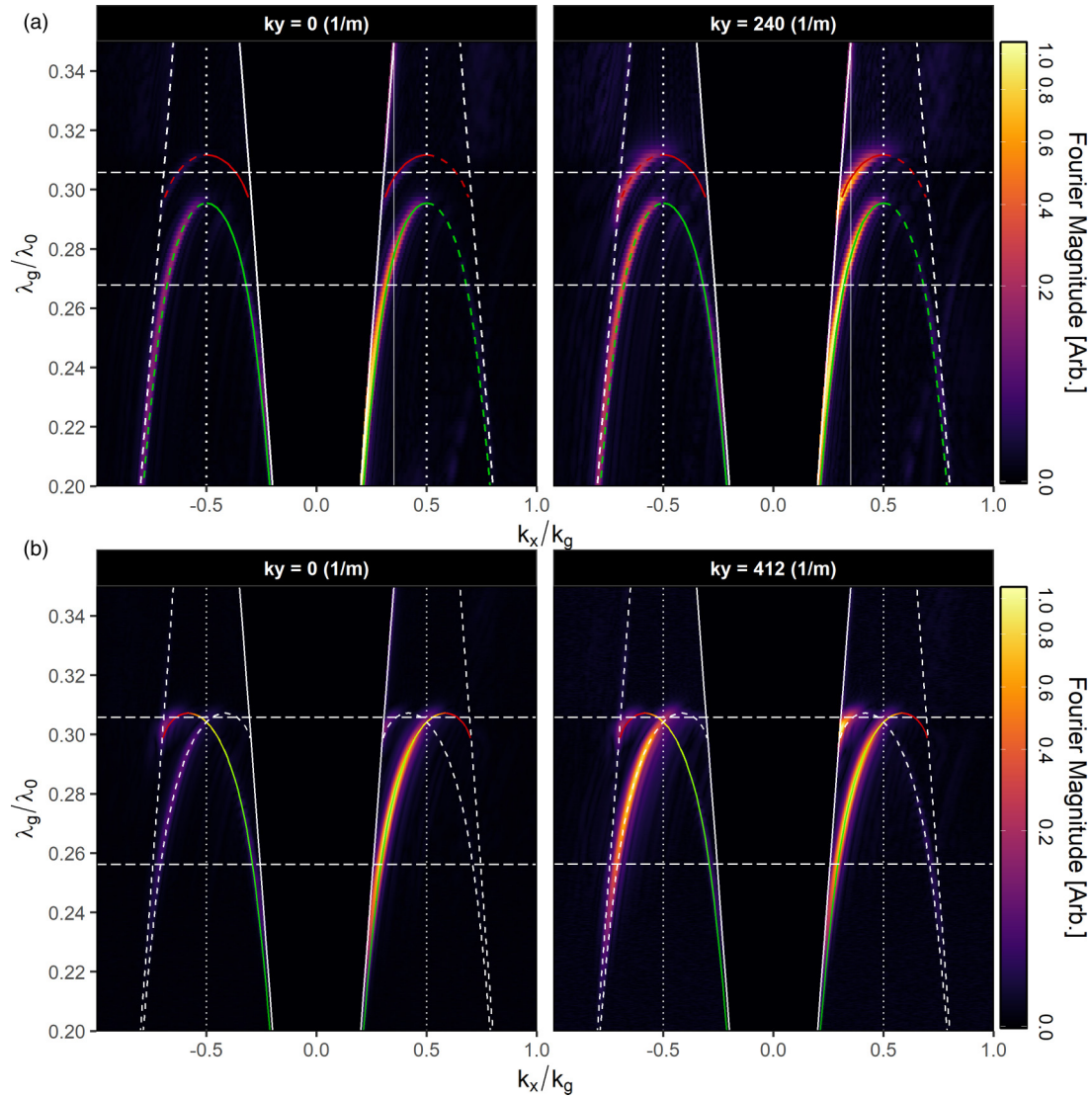


FIG. 5. Dispersion diagrams calculated from the experimental data at two different cross sections of  $k$ -space wave vector  $k_y$  (labeled) for (a) sample A and (b) sample B. The ratio of grating pitch to free-space wavelength  $\frac{\lambda_g}{\lambda_0}$  is plotted as a function of reduced in-plane wave vector  $\frac{k_x}{k_g}$ . Solid lines represent sound line  $k_0$ , dashed lines their diffracted counterparts  $\pm k_0 \pm nk_g$ . Vertical dotted lines represent the first Brillouin zone boundaries  $\pm \frac{mk_g}{2}$ , and horizontal dot dashed lines the frequencies at which Figs. 3 and 4 are plotted. In both plots, eigenfrequency predictions of a loss-inclusive numerical model are overlaid as colored lines. Green represents the even modes, red the odd modes. A solid line is a mode that has not undergone diffraction from  $\pm k_g$ , a dashed line is one that has.

occur at a position directly in line with the locations of the pressure node on the adjacent line of holes, and vice versa, acting to cancel them out.

The  $k_y$ -dependent diffraction is again clear in the high-frequency  $k$ -space plot in Fig. 3(b). Here, there are now two modes visible in the positive half of the first BZ ( $0 < k_x < k_g/2$ ) at one frequency, a result of the band gap and standing wave pair not forming at the edge of this first BZ. There is a bright feature occurring at the first BZB,  $k_x = k_g/2$ , and another feature just outside  $k_0$  whose amplitude falls to zero with no  $k_y$  component. In the second BZ of the negative half of  $k$ -space ( $-k_g < k_x < -k_g/2$ ), this behavior is reversed; the feature at the first BZB has a null at  $k_y = 0$ , and a feature with a maximum at  $k_y = 0$  is apparent just outside of the first diffracted sound circle  $-k_0$ . This is a result of the hybrid

ALM forming a standing wave at an arbitrary value of  $k_x$  between the two features, and the curvature of the mode thus changing its sign: part of it appears to disperse negatively. Hence, a feature appears in the negative half of  $k$  space which corresponds to the region of negative dispersion that is excitable on the mode originating at  $k_x = 0$  but propagating in the negative  $x$  direction. The equivalent segment of the mode traveling in the positive direction is in contrast not visible, as its negative group velocity means power does not flow from the source to the detector. This behavior is easier to understand with inspection of the corresponding dispersion relations.

Marked in Figure 4(b) as vertical dot-dashed lines are the values of  $k_y$  used to create the two cross sections of  $k$  space in all panels of Fig. 5, necessary to show the dispersion

of both the even and odd modes. Note the sudden drop in the amplitude of the mode expected at  $k_y/k_g = 0$  is slightly shifted toward negative  $k_y$ —this is the result of the sample not being perfectly aligned in either one or both of the  $xy$  and  $yz$  planes, and the resolution of  $k_y$  ( $\Delta k_y$ ) not being high enough to prevent fast Fourier transform (FFT) spectral leakage [47].

Experimentally derived dispersion plots are shown in Fig. 5 and compared with the results of a loss-inclusive finite element method (FEM) model overlaid as colored lines. Briefly, the model results are the calculated eigenmodes of the ASWs supported by the sample. The system is modeled as a unit cell with periodic conditions in the  $x$  direction (see Fig. 1) bound by perfectly matched layers in the  $y$  and  $z$  directions. This approximates the sample as a periodically perforated plate with infinite extent in the  $x$  direction, with a width  $D_{A|B}$  in the  $y$  dimension, surrounded by air extending indefinitely (further details provided in Appendix B). Loss arising from thermoviscous boundary layers are captured in the model. For the cavities studied here, the thermal and viscous boundary layers do not give rise to significant losses since the occupancy of the layers relative to the cavity diameters is small (here the thermal,  $\delta_t$ , and viscous,  $\delta_v$ , boundary layer thicknesses are approx. 12  $\mu\text{m}$  and 16  $\mu\text{m}$ , respectively, at 10 kHz). These boundary layers give rise to a small reduction  $\Delta f = 0.2$  kHz in resonance frequency due to a change in the effective velocity of sound in the cavity [48].

Cross sections of  $k$  space at two values of  $k_y$  are included to further demonstrate the strong dependence on  $k_y$  of the high-frequency odd mode while the low-frequency even mode does not change significantly with  $k_y$ .

Figure 5(a) (left) displays the dispersion of the low-frequency mode on sample A originating at  $k_x = 0$  (represented by green solid lines calculated from the numerical model in both positive and negative  $k$  space) follows the expected [4,13,16,44] pattern. At low frequencies, this mode occurs very near the sound line  $k_0 = 2\pi f/c$  and is thus indistinguishable from a grazing sound wave. As the frequency increases, the ALM gradually increases its wave vector in  $x$  beyond  $k_0$ , becoming a fully trapped surface mode, until at the first BZB at  $k_x/k_g$ , its group velocity falls to zero and forms a standing-wave along  $x$ .

In the dispersion plot taken from a cross section of  $k$  space at  $k_y = 0$ , the high-frequency odd mode is barely visible as a feature, since it requires a component of  $k_y$  to be excited (and as mentioned, is only visible at all due to imperfections in sample alignment and lack of  $k_y$  resolution). When the cross section is taken at the nonzero value of  $k_y$  marked in Fig. 4(a), the odd mode appears as a well-defined feature at high frequency (solid red lines, with its diffracted counterparts marked by dashed red lines). Since this mode originates in the first BZ due to not having the necessary degrees of freedom available along  $x$ , it disperses positively, with behavior almost identical to that of the low-frequency even mode. Also, instead of following the sound line  $k_0$  at low frequency, it appears to cease to exist in the nonradiative regime, instead crossing the sound line at some finite frequency: the pair of holes acts like a waveguide along  $x$  with a cutoff frequency dictated by the hole separation in  $y$ . The model predicts that this odd mode would continue to exist in the radiative regime, but that was not measured in this experiment.

The equivalent dispersion diagrams are shown for the glide case, sample B, in Fig. 5(b) with cross sections through  $k_y$  indicated by vertical dot-dashed lines in Fig. 4(b), with appropriate features labeled as before. Again, colored lines represent the prediction of a loss-inclusive FEM model, the choice of color and line type dependent on the character of the mode they represent, to be discussed.

What is striking about this dispersion compared to that of sample A is that for both  $k_y$  cross sections, there are no longer two distinct modes with a clear separation in frequency. Instead, the low-frequency nondiffracted (or non-band-folded) mode that previously formed a standing wave at  $k_x/k_g = 0.5$  and  $\lambda_g/\lambda_0 = 0.28$  (green lines in Fig. 5) continues to rise in frequency and  $k_x$  beyond the first BZB until its group velocity eventually falls to zero at  $k_x/k_g \approx 0.6$ . The limit imposed by the lack of degrees of freedom in the  $x$  direction of the unit cell in sample A is removed, as the shift of the second row of holes along  $x$  has created an extra degree of freedom. The change in mode symmetry is marked by a numerically calculated solid line whose color changes from green to red, highlighting the changing character of the hybrid surface mode from mostly even at low frequency to mostly odd at high frequency.

At  $\lambda_g/\lambda_0 = 0.28$ , a second feature has appeared at a lower wave vector than the nondiffracted mode, whose origin is understood by comparing the two  $k_y$  cross sections. For the cross section at  $k_y/k_g = 0$ , this second feature appears only as a weak feature just outside the sound line in the positive half of  $k$  space, the same character that the high-frequency odd mode had for sample A (Fig. 5, red lines). However, the low-frequency mode associated with diffraction from  $-k_g$  is simultaneously weakened (marked by the changing-color dashed line in the negative half of  $k_x$ ), suggesting that the two features are linked. Indeed, there is another feature above this diffracted mode visible just below the  $k_0 - k_g$  sound line, which has similar strength in both cross sections of  $k$  space, and which Fig. 5(b) showed did not have a minimum at  $k_y/k_g = 0$ : this feature is associated with the mode excitable at  $-k_0$  existing in the negative half of  $k$  space that has *not* been diffracted (again, marked by a changing-color solid line).

Beyond the  $k_x$  value at which the nondiffracted ALM excited in the positive half of  $k$ -space (solid line) has formed a standing wave at an arbitrary wave vector, its gradient changes signs, and it continues to evolve with a negative group velocity. Hence this region of the mode's band structure ceases to be excitable. In the negative half of  $k_x$ , this same negatively dispersing region of the other non-diffracted mode has become excitable, as relative to the source, it now has a positive group velocity. With the same argument, the equivalent feature in the positive half of  $k$ -space is associated with the negatively dispersing branch of the mode diffracted from  $-k_g$ , requiring a component of  $k_y$  to be excited (hence represented by the dashed line). Thus, on the glide-symmetry sample there is a frequency band where the ALM appears to be dispersing negatively, as observed by Queseda *et al.* [39] in an electromagnetic waveguide. However, this region of the mode dispersion is not truly negative index, as the ASW fundamentally arises from diffraction. Note, as with the previous sample, weak coupling to the mode existing within

the first BZ of negative  $k$  space occurs because of reflections from the sample edge. Also, the cross section through  $k_y/k_g = 0$  is not quite at zero due to imperfections in sample alignment.

In summary then, the effect of the glide symmetry is to remove the distinction between the even and odd character modes, creating one ALM with mixed character; at low frequencies, it appears more evenlike, at high frequencies, it appears more oddlike. Also, a new standing wave is formed at an arbitrary point in  $k_x$ , beyond the first BZ, where the group velocity changes sign and thus the ALM appears to disperse negatively. This behavior is analogous to that predicted by Hessel *et al.* [38] and observed by Quesada *et al.* [39] for an electromagnetic waveguide with glide-symmetry. The  $k_x$  value of the standing wave that now forms is determined nontrivially via the Fourier coefficients of the structure factor, as it results from the balance between forward- and backscattered ALMs that do not have to obey the symmetry conditions usually imposed at the first BZ boundary.

## V. CONCLUSIONS

The paper presented here investigated the effect of glide symmetry on ASWs that take the form of ALMs [36]. Glide-symmetry refers to a kind of symmetry where a periodic system's unit-cell is inverted along its  $y$  axis midplane, and then one side translated by exactly half of the grating periodicity, such as in a zigzag [38]. Two samples were characterized using a high-resolution acoustic near-field measuring technique, whereby high-quality 2D pressure field maps can be created, then via spatial Fourier transforms, the dispersion of any present trapped surface modes extracted. The first sample consisted of two line arrays arranged side by side, completely symmetric about a mirror plane in  $y$ , where two separate modes were found to exist: a low-frequency mode whose fields had phase symmetry about  $y$ , i.e., having even character, and a high-frequency mode whose field's phase was antisymmetric about  $y$ , i.e., having odd character. Both modes had broadly the same characteristics of the air-bound ASWs previously investigated [4,13,16,44], each forming a standing wave at the first BZ boundary. The second sample was similar to the first, except one line of holes was translated along  $x$  by half of the width of a unit cell, thereby creating glide symmetry. As a result, it was observed that the previously distinct even and odd modes became mixed, and at the first BZ boundary, a standing wave was no longer formed, rather the mode exhibits gapless dispersion through the first BZ. Instead, the standing wave is formed at an arbitrary value of in-plane wave vector determined nontrivially by the Fourier components of the unit-cell structure factor, as a generalized theory for the electromagnetic case constructed by Hessel *et al.* also predicted [38]. The resulting change in sign of the group velocity of the mode appeared to create a region of negative dispersion, as measured by Quesada *et al.* [39] in a similar electromagnetic system, though it is not really negative index as it fundamentally arises from a diffraction effect. Finally, this paper has shown how the simple addition of glide symmetry to a system can allow for an improved

degree of control over the dispersion of an ASW, namely, the removal of the band gap at the first BZ boundary, enabling mode dispersion through the BZB. This provides a route to tailoring the propagation of sound on surfaces using passive structure, which could be useful for the design of acoustic devices.

The research data supporting this publication are openly available from the University of Exeter's institutional repository at Ref. [50].

## ACKNOWLEDGMENT

The authors would like to thank DSTL for their financial support.

## APPENDIX A: EXPERIMENTAL CHARACTERIZATION

Acoustic measurements of the surface wave pressure field used a fixed loudspeaker source and a detector on the opposite side of the sample on a translation stage. Acoustic surface modes were excited using a modified Tucker-Davis Technologies MF1 near-field source positioned over a hole in the center of the sample to diffractively couple sound to the surface modes. This source was excited with single cycle sine-Gaussian waveform with 16 kHz carrier frequency.

A Brüel & Kjær type 4182 needle-tip probe microphone positioned on the opposite side of the sample was raster scanned in a plane approximately 1 mm above the sample surface using the translation stage.

At each spatial point, the time-dependent signal (voltage) is recorded with a sampling frequency of 312.5 kHz for a duration of 32 ms. The detecting microphone was scanned to produce data in the XY plane with resolution  $\Delta x = \Delta y = 0.5$  mm. The momentum-space resolution of this experiment is limited by the scan length,  $\Delta k = 1/x_{\max}$ , and the range is limited by the minimum scan step size,  $\Delta x$  (maximum wave vector  $k_{\max} = 2\pi/\Delta x$ ).

## APPENDIX B: NUMERICAL MODEL

Surface mode dispersion was calculated using the FEM modeling package, COMSOL MULTIPHYSICS (version 5.3a) with pressure acoustic and thermoacoustic modules. The dispersion relations presented are the eigenmodes of the unit cell presented in Fig. 1. The unit cell comprises holes (cylindrical cavities) perforated through a plate of thickness,  $H$ , and width,  $D$ , in the  $z$  and  $y$  directions, respectively, with Floquet-Periodic boundary conditions in the  $x$  direction to represent a periodic line of open cavities of infinite extent. The plate is treated as sound hard; the acoustic field is not solved in the solid. Acoustic loss that arises due to the no-slip and isothermal boundary condition at the fluid-solid interfaces within the cavities are accounted for by solving the constitutive equations and the linearized Navier-Stokes equations. The properties of air were taken from Ref. [49] and are assumed as density  $\rho = 1.2$  kg/m<sup>3</sup>, velocity of sound  $c_s = 343.2$  ms<sup>-1</sup>, dynamic viscosity  $\mu_B = 15.6 \times 10^{-8}$  Pa s, at  $T = 293.15$  K.

An illustrative COMSOL model is openly available as part of the research data in Ref. [50].



- [1] S. B. Glybovski, S. A. Tretyakov, P. A. Belov, Y. S. Kivshar, and C. R. Simovski, *Metasurfaces: From microwaves to visible*, *Phys. Rep.* **634**, 1 (2016).
- [2] G. Ma and P. Sheng, Acoustic metamaterials: From local resonances to broad horizons, *Sci. Adv.* **2**, e1501595 (2016).
- [3] S. A. Cummer, J. Christensen, and A. Alù, Controlling sound with acoustic metamaterials, *Nat. Rev. Mater.* **1**, 16001 (2016).
- [4] J. Christensen, L. Martín-Moreno, and F. J. García-Vidal, Theory of Resonant Acoustic Transmission Through Subwavelength Apertures, *Phys. Rev. Lett.* **101**, 014301 (2008).
- [5] Y. Ye, M. Ke, Y. Li, T. Wang, and Z. Liu, Focusing of spoof surface-acoustic-waves by a gradient-index structure, *J. Appl. Phys.* **114**, 154504 (2013).
- [6] K. M. Ivanov-Shits and F. V. Rozhin, Investigation of surface waves in air, *Sov. Phys. Acoust.* **5**, 510 (1959).
- [7] A. R. Wenzel, Propagation of waves along an impedance boundary, *J. Acoust. Soc. Am.* **55**, 956 (1974).
- [8] T. F. Embleton, J. E. Piercy, and N. Olson, Outdoor sound propagation over ground of finite impedance, *J. Acoust. Soc. Am.* **59**, 267 (1976).
- [9] J. Pendry, L. Martín-Moreno, and F. García-Vidal, Mimicking surface plasmons with structured surfaces, *Science* **305**, 847 (2004).
- [10] A. P. Hibbins, B. R. Evans, and J. R. Sambles, Experimental verification of designer surface plasmons, *Science* **308**, 670 (2005).
- [11] W. L. Barnes, T. W. Preist, S. C. Kitson, and J. R. Sambles, Physical origin of photonic energy gaps in the propagation of surface plasmons on gratings, *Phys. Rev. B* **54**, 6227 (1996).
- [12] Y. V. Gulyaev and V. P. Plesskii, Propagation of acoustic surface waves in periodic structures, *Sov. Phys. Usp.* **32**, 51 (1989).
- [13] B. Hou, J. Mei, M. Ke, W. Wen, Z. Liu, J. Shi, and P. Sheng, Tuning Fabry-Perot resonances via diffraction evanescent waves, *Phys. Rev. B* **76**, 054303 (2007).
- [14] L. Kelders, J. F. Allard, and W. Lauriks, Ultrasonic surface waves above rectangular-groove gratings, *J. Acoust. Soc. Am.* **103**, 2730 (1998).
- [15] D. Torrent and J. Sánchez-Dehesa, Acoustic Analogue of Graphene: Observation of Dirac Cones in Acoustic Surface Waves, *Phys. Rev. Lett.* **108**, 174301 (2012).
- [16] X. Wang, Theory of resonant sound transmission through small apertures on periodically perforated slabs, *J. Appl. Phys.* **108**, 064903 (2010).
- [17] J. G. Beadle, I. R. Hooper, J. R. Sambles, and A. P. Hibbins, Broadband, slow sound on a glide-symmetric meander-channel surface, *J. Acoust. Soc. Am.* **145**, 3190 (2019).
- [18] T. A. Starkey, V. Kyrimi, G. P. Ward, J. R. Sambles, and A. P. Hibbins, Experimental characterisation of the bound acoustic surface modes supported by honeycomb and hexagonal hole arrays, *Sci. Rep.* **9**, 15773 (2019).
- [19] T. J. Graham, A. P. Hibbins, J. R. Sambles, and T. A. Starkey, Underwater acoustic surface waves on a periodically perforated metal plate, *J. Acoust. Soc. Am.* **146**, 4569 (2019).
- [20] N. Korozlu, O. A. Kaya, A. Cicek, and B. Ulug, Self-collimation and slow-sound effect of spoof surface acoustic waves, *J. Appl. Phys.* **125**, 074901 (2019).
- [21] A. A. Maradudin, Surface electromagnetic waves on structured perfectly conducting surfaces, in *Modern Plasmonics*, Handbook of Surface Science, Vol. 4, edited by A. A. Maradudin, J. R. Sambles, and W. L. Barnes (North-Holland, Oxford, 2014), pp. 223–251.
- [22] A. P. Hibbins, M. J. Lockyear, and J. R. Sambles, The resonant electromagnetic fields of an array of metallic slits acting as Fabry-Perot cavities, *J. Appl. Phys.* **99**, 124903 (2006).
- [23] C. Kittel and D. F. Holcomb, Introduction to solid state physics, *Am. J. Phys.* **35**, 547 (1967).
- [24] M. H. Lu, X. K. Liu, L. Feng, J. Li, C. P. Huang, Y. F. Chen, Y. Y. Zhu, S. N. Zhu, and N. B. Ming, Extraordinary Acoustic Transmission Through a 1D Grating with Very Narrow Apertures, *Phys. Rev. Lett.* **99**, 174301 (2007).
- [25] Y. Zhou, M.-H. Lu, L. Feng, X. Ni, Y.-F. Chen, Y.-Y. Zhu, S.-N. Zhu, and N.-B. Ming, Acoustic Surface Evanescent Wave and Its Dominant Contribution to Extraordinary Acoustic Transmission and Collimation of Sound, *Phys. Rev. Lett.* **104**, 164301 (2010).
- [26] J. Zhu, J. Christensen, J. Jung, L. Martín-Moreno, X. Yin, L. Fok, X. Zhang, and F. García-Vidal, A holey-structured metamaterial for acoustic deep-subwavelength imaging, *Nat Phys.* **7**, 52 (2011).
- [27] H. Jia, M. Lu, Q. Wang, M. Bao, and X. Li, Subwavelength imaging through spoof surface acoustic waves on a two-dimensional structured rigid surface, *Appl. Phys. Lett.* **103**, 103505 (2013).
- [28] J. Christensen, L. Martín-Moreno, and F. J. García-Vidal, Enhanced acoustical transmission and beaming effect through a single aperture, *Phys. Rev. B* **81**, 174104 (2010).
- [29] J. Cui, J. Liu, Y. Mao, Y. Li, and X. Liu, Realization of manipulating acoustic surface waves radiation direction with rectangular-groove structure, *AIP Adv.* **7**, 115301 (2017).
- [30] H. Estrada, P. Candelas, A. Uris, F. Belmar, F. Meseguer, and F. J. García de Abajo, Sound transmission through perforated plates with subwavelength hole arrays: A rigid-solid model, *Wave Motion* **48**, 235 (2011).
- [31] M. Mazzotti, M. Miniaci, and I. Bartoli, Band structure analysis of leaky Bloch waves in 2D phononic crystal plates, *Ultrasonics* **74**, 140 (2017).
- [32] H. Estrada, P. Candelas, F. Belmar, A. Uris, F. J. García de Abajo, and F. Meseguer, Engineering surface waves in flat phononic plates, *Phys. Rev. B* **85**, 174301 (2012).
- [33] N. Cselyszka, M. Sečujski, N. Engheta, and V. Crnojević-Bengin, Temperature-controlled acoustic surface waves, *New J. Phys.* **18**, 103006 (2016).
- [34] N. Cselyszka, N. Janković, A. Alu, and V. Bengin, Acoustic spoof surface waves control in corrugated surfaces and their applications, in *Metamaterials: Technology and Applications*, 1st ed., edited by P. K. Choudhury (CRC Press, Taylor and Francis Group, Boca Raton, 2022), Chap. 11, pp. 289–312.
- [35] S. Damani, E. Totten, L. Davies, W. N. Alexander, W. J. Devenport, B. P. Pearce, S. R. Shelley, T. A. Starkey, A. P. Hibbins, and J. R. Sambles, Excitation of airborne acoustic surface modes driven by a turbulent flow, *AIAA J.* **59**, 5011 (2021).
- [36] G. P. Ward, A. P. Hibbins, J. R. Sambles, and J. D. Smith, The waveguiding of sound using lines of resonant holes, *Sci. Rep.* **9**, 11508 (2019).
- [37] D. Colquitt, R. V. Craster, T. Antonakakis, and S. Guenneau, Rayleigh-Bloch waves along elastic diffraction gratings, *Proc. R. Soc. A* **471**, 20140465 (2015).

- [38] A. Hessel, M. H. Chen, R. C. Li, and A. A. Oliner, Propagation in periodically loaded waveguides with higher symmetries, *Proc. IEEE* **61**, 183 (1973).
- [39] R. Quesada, D. Martín-Cano, F. García-Vidal, and J. Bravo-Abad, Deep-subwavelength negative-index waveguiding enabled by coupled conformal surface plasmons, *Opt. Lett.* **39**, 2990 (2014).
- [40] N. Janković and A. Alù, Glide-symmetric acoustic waveguides for extreme sensing and isolation, *Phys. Rev. Appl.* **15**, 024004 (2021).
- [41] O. Quevedo-Teruel, Q. Chen, F. Mesa, N. J. G. Fonseca, and G. Valerio, On the benefits of glide symmetries for microwave devices, *IEEE J. Microw.* **1**, 457 (2021).
- [42] R. McWeeny, *Symmetry: An Introduction to Group Theory and its Applications* (Courier Corporation, Oxford, 2002).
- [43] T. J. Constant, T. S. Taphouse, H. J. Rance, S. C. Kitson, A. P. Hibbins, and J. R. Sambles, Surface plasmons on zig-zag gratings, *Opt. Express* **20**, 23921 (2012).
- [44] G. P. Ward, A. P. Hibbins, J. R. Sambles, and J. D. Smith, Acoustic transmission through compound subwavelength slit arrays, *Phys. Rev. B* **94**, 024304 (2016).
- [45] D. C. Skigin and R. A. Depine, Transmission Resonances of Metallic Compound Gratings with Subwavelength Slits, *Phys. Rev. Lett.* **95**, 217402 (2005).
- [46] A. P. Hibbins, I. R. Hooper, M. J. Lockyear, and J. R. Sambles, Microwave Transmission of a Compound Metal Grating, *Phys. Rev. Lett.* **96**, 257402 (2006).
- [47] L. R. Rabiner and B. Gold, *Theory and Application of Digital Signal Processing*, 1st ed. (Prentice-Hall Inc., Englewood Cliffs, NJ, 1975).
- [48] G. P. Ward, R. K. Lovelock, A. R. J. Murray, A. P. Hibbins, J. R. Sambles, and J. D. Smith, Boundary-Layer Effects on Acoustic Transmission Through Narrow Slit Cavities, *Phys. Rev. Lett.* **115**, 044302 (2015).
- [49] O. Cramer, The variation of the specific heat ratio and the speed of sound in air with temperature, pressure, humidity, and CO<sub>2</sub> concentration, *J. Acoustic. Soc. Am.* **93**, 2510 (1993).
- [50] <https://doi.org/10.24378/exe.4023>.